






RESEARCH ARTICLE | JANUARY 31 2024

Modeling, properties, and fabrication of a micromachined thermoelectric generator

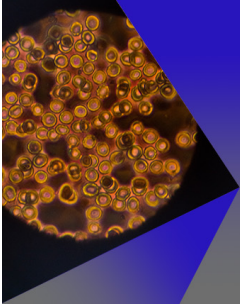
Hartmut Uebensee; Manfred Reiche ; Hans Kosina; Xuemei Xu; Hartmut S. Leipner; Geert Brokmann ; Bernhard Schwartz ; Anna Reinhardt ; Thomas Ortlepp 



AIP Advances 14, 015165 (2024)
<https://doi.org/10.1063/5.0179769>




CrossMark



AIP Advances
Special Topic: Medical Applications
of Nanoscience and Nanotechnology

Submit Today!



Modeling, properties, and fabrication of a micromachined thermoelectric generator

Cite as: AIP Advances 14, 015165 (2024); doi: 10.1063/5.0179769

Submitted: 8 November 2023 • Accepted: 13 December 2023 •

Published Online: 31 January 2024



Hartmut Uebensee,¹ Manfred Reiche,^{1,a)} Hans Kosina,² Xuemei Xu,¹ Hartmut S. Leipner,³ Geert Brokmann,¹ Bernhard Schwartz,¹ Anna Reinhardt,¹ and Thomas Ortlepp¹

AFFILIATIONS

¹CIS Forschungsinstitut für Mikrosensorik GmbH, Konrad-Zuse-Str. 14, D-99099 Erfurt, Germany

²Institut für Mikroelektronik, Technische Universität Wien, Gusshausstr. 27-29, A-1040 Vienna, Austria

³Martin-Luther-Universität Halle-Wittenberg, Nanotechnikum Weinberg, Heinrich-Dammerow-Str. 4, D 06120 Halle, Germany

^{a)}Author to whom correspondence should be addressed: mreiche@cismst.de

ABSTRACT

Different electrical and thermoelectric properties of a Si-based thermoelectric generator (TEG) are described based on the Kubo–Greenwood formalism. Temperature and doping dependence, phonon scattering (acoustic and optical phonons), and scattering on impurities are included. Comparisons with experimentally verified data confirm the validity of the model. Experimental studies were carried out on a micromechanically fabricated TEG. Devices were realized using a standard CMOS SOI technology in a lateral geometry. All thermopiles are located on a thin membrane to reduce the heat flow. The thickness of the membrane was adjusted between 20 and 30 μm ensuring also sufficient mechanical stability. Measurements on individual devices confirm the results of the theoretical model. The Seebeck coefficient was calculated and experimentally measured as $S = 0.5 \text{ mV/K}$ at an acceptor level of 10^{19} cm^{-3} at room temperature. The power factor is $S^2 \cdot \sigma = 0.0073 \text{ W/mK}^2$.

© 2024 Author(s). All article content, except where otherwise noted, is licensed under a Creative Commons Attribution (CC BY) license (<http://creativecommons.org/licenses/by/4.0/>). <https://doi.org/10.1063/5.0179769>

I. INTRODUCTION

Thermoelectric generators (TEGs) are attractive as an environmentally clean technology for converting waste heat into electric power. Bulk TEGs are used to generate power from heat sources, such as power plants or vehicle engines.^{1,2} Recently, microelectronic thermoelectric devices gained importance for near-room-temperature waste heat harvesting in numerous integrated circuit and sensor applications.^{3–5} Such applications mainly require silicon as a construction material. However, it is known that silicon is not an ideal thermoelectric material. Caused by the high thermal conductivity (about 140 W/mK at room temperature), the value of ZT is about 10^{-3} to 10^{-2} near room temperature. The figure-of-merit is $ZT = (\sigma S^2 / \kappa) T$, where σ is the electrical conductivity, S is the Seebeck coefficient, κ is the thermal conductivity, and $T = 1/2(T_H + T_C)$ with T_H being the hot temperature and T_C being the cold temperature (in K) across the TEG. Attempts to increase Si thermoelectric efficiency have been mostly pursued by decreasing its thermal conductivity. Dimensional constraints were shown to be effective to reduce κ .⁶

The damping of thermal conductivity by incoherent phonon scattering at silicon nanowire walls was found capable of reducing Si thermal conductivity by almost two orders of magnitude at room temperature.^{7,8} These findings have stimulated numerous efforts to develop microelectronic TEGs with silicon nanowires or other micro- or nanostructured Si thermopiles (for more recent reviews, see Refs. 4, 5, 9 and 10) and to explanations by numerical simulations and theory (for instance, Refs. 11 and 12). However, it was demonstrated that the thermopile characteristics and efficiencies of such nanostructured Si TEGs are considerably smaller than primarily reported.^{9,13} Therefore, the power factor that is the product σS^2 in the numerator of ZT becomes more important. The electrical conductivity and Seebeck coefficient increase significantly by applying heavily doped Si and consequently result in an increase of ZT . This was evidenced by several experimental and theoretical studies.^{14–16}

Another critical requirement for microelectronic thermoelectric devices to achieve a high level of acceptance is reduced fabrication cost and integrability into microelectronic or micromechanic

process flows.^{13,17} Examples combining sufficiently high power factors with integrability have been already demonstrated.^{5,18,19} This paper deals with a theoretical model regarding, especially, a high boron doping and with experimental studies of a micromechanically fabricated TEG to prove the results of the model.

II. THEORETICAL MODEL

Different approaches (Monte Carlo simulations, quantum non-equilibrium Green's function, *ab initio* methods, etc.) have been used to describe thermoelectric parameters, such as the figure-of-merit, Seebeck coefficient, and power factor.^{20–27} Here, the Kubo–Greenwood formalism^{28,29} is used. The electrical conductivity σ and Seebeck coefficient S within this formalism are

$$\vec{\sigma} = -\frac{e^2}{4\pi^3} \int \tau(E) \vec{\sigma}(E) \frac{\partial f_0}{\partial E} dE$$

with

$$\vec{\sigma}(E) = \int \vec{v}(\vec{k}) \otimes \vec{v}(\vec{k}) \frac{dA}{\hbar |\vec{v}(\vec{k})|}, \quad (1)$$

$$\vec{S} = \frac{1}{\sigma_0} \int \tau(E) \vec{\sigma}(E) \frac{E(\vec{k}) + E_0 - E_F(\vec{r})}{T} \left(-\frac{\partial f_0}{\partial E} \right) dE. \quad (2)$$

Note that $\vec{\sigma}$ and \vec{S} are the tensors of second order. In Eqs. (1) and (2), \vec{k} indicates the wave vector and $\vec{v}(\vec{k})$ is the vector of group velocity resulting from band structure,

$$\vec{v}(\vec{k}) = \frac{1}{\hbar} \nabla_{\vec{k}} E(\vec{k}), \quad (3)$$

where E is the energy, E_0 is the zero-point energy, f_0 is the Fermi distribution, and τ is the relaxation time. Band structure calculations were carried out either by empiric pseudopotential method (EPM) using the method described in Refs. 30 and 31 or by a $\mathbf{k} \cdot \mathbf{p}$ (6×6)-model.³² For boron-doped silicon, the carriers are holes, i.e., all three valence bands (heavy hole band, light hole band, and split-off band) are included.

For bulk materials, as in our case, the relaxation time is assumed to be isotropic and, therefore, depends only on E . Contrary to a previous paper,³³ we consider parts for scattering of acoustic phonons, nonpolar optical phonons, and scattering on ionized impurities individually for each valence band according to Matthiessen's rule. In the literature, different expressions are given for different scattering parts.^{33–35} Introducing the density of states as integral over an isoenergy surface,

$$D(E) = \frac{2}{(2\pi)^3} \int \frac{dA_{surf}}{|\nabla_{\vec{k}} E(\vec{k})|}, \quad (4)$$

it can be shown that different expressions for individual scattering rates are equivalent.³⁶ In Eq. (4), dA_{surf} means the surface element.

Scattering on acoustic phonons is then given as³³

$$\frac{1}{\tau_{aph}} = \frac{2\pi D_{aph}^2 k_B T}{\hbar \rho v_{th}^2} D(E), \quad (5)$$

where D_{aph} is the acoustic deformation potential, \hbar is the reduced Planck constant, ρ is the mass density, k_B is the Boltzmann constant, and v_{th} is the velocity of sound (8433 m/s for longitudinal waves).

Since we are dealing with near-equilibrium hole transport, it is sufficient to consider the asymptotic behavior of $D(E)$ at small energies, which is $E^{1/2}$ for a three-dimensional system. Using this approximation, Eq. (5) can be rewritten as³⁵

$$\frac{1}{\tau_{aph}} = \frac{1}{\tau_{aph0}} \frac{T}{T_0} \sqrt{\frac{E - E_0}{k_B T_0}}, \quad (6)$$

with

$$\frac{1}{\tau_{aph0}} = \frac{D_{aph}^2 (2m_{eff} m_e k_B T)^{3/2}}{4\pi \hbar^4 c_L}, \quad (7)$$

where m_{eff} is the density-of-state effective mass of each valence band, $T_0 = 300$ K, and $c_L = \rho \cdot v_{th}^2$.

Scattering on nonpolar optical phonons is described as³⁴

$$\frac{1}{\tau_{oph}} = \frac{1}{\tau_{oph0}} \left(N_q \sqrt{\frac{E - E_0 + \hbar\omega_0}{k_B T_0}} + (N_q + 1) \times \sqrt{\frac{E - E_0 - \hbar\omega_0}{k_B T_0}} \Theta(E - E_0 - \hbar\omega_0) \right), \quad (8)$$

with

$$\frac{1}{\tau_{oph0}} = \frac{D_{oph}^2 (m_{eff} m_e)^{3/2} \sqrt{k_B T_0}}{\sqrt{2\pi} \hbar^3 \rho \omega_0} \quad (9)$$

and

$$N_q = \frac{1}{\exp\left(\frac{\hbar\omega_0}{k_B T}\right) - 1}. \quad (10)$$

D_{oph} is the optical deformation potential and $\hbar\omega_0 = 63$ meV.

Assuming full ionization, the scattering on ionized impurities is given as³³

$$\frac{1}{\tau_{ion}} = \frac{1}{\tau_{ion0}} \frac{k_0^4 N_A}{k^4 N_0} \sqrt{\frac{E(k) - E_0}{k_B T_0}} \cdot L(2\lambda_D k), \quad (11)$$

with

$$\tau_{ion0} = \left(\frac{1}{2\pi} \frac{e^4 \cdot N_0 \cdot (m_{eff} m_e)^{3/2} \cdot \sqrt{k_B T_0}}{\hbar^4 \cdot k_0^4 (\epsilon_{Si} \cdot \epsilon_0)^2} \right)^{-1}. \quad (12)$$

Here, the function $L(x)$ is

$$L(x) = \ln(1 + x^2) - \frac{x^2}{1 + x^2}, \quad x = 2\lambda_D k. \quad (13)$$

with

$$E(k) = E_0 + \frac{\hbar^2 k^2}{2m_{eff} m_e}, \text{ the wave vector,}$$

$$k = \sqrt{\frac{2m_{eff} m_e}{\hbar^2} (E(k) - E_0)} \text{ and } \lambda_D \text{ as the Debye length,}$$

$$\lambda_D^{-2} = \frac{e^2}{\epsilon_{Si} \epsilon_0 k_B T} \left| \frac{\partial p}{\partial E_F} \right| \approx \frac{e^2 N_A}{\epsilon_{Si} \epsilon_0 k_B T} \frac{F_{-1/2}(E_F)}{F_{1/2}(E_F)}, \quad (14)$$

where p is the hole density, ϵ_{Si} is the silicon dielectric constant, $k_0 = 0.1 \text{ nm}$, N_A is the acceptor concentration, and $N_0 = 10^{17} \text{ cm}^{-3}$. Contrary to previous papers (e.g., Ref. 33), incomplete ionization is assumed and N_A is replaced by N_A^- characterizing only the part of ionized acceptors,³⁷

$$N_A^- = \frac{N_A}{1 + \frac{1}{g} \exp\left(\frac{E_A - E_F}{kT}\right)}, \quad (15)$$

where g is the ground state degeneracy factor that is 4 for acceptors.

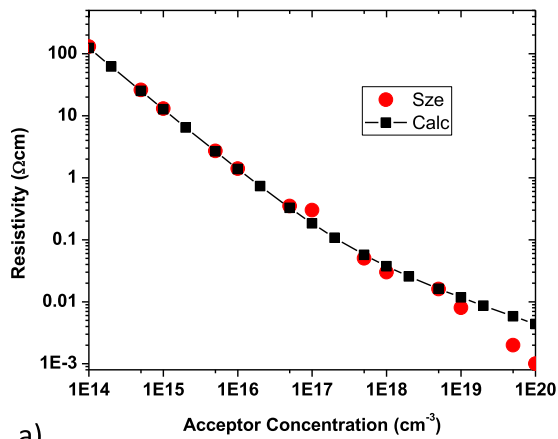
The temperature- and doping-depended Fermi levels were deduced based on charged neutrality,

$$\frac{N_A}{1 + \frac{1}{g} \exp\left(\frac{E_A - E_F}{kT}\right)} = p^{hh} + p^{lh} + p^{so} = \sum_{xx=hh, lh, so} \int_{E_{xx}}^{-\infty} dE D(E) f_0, \quad (16)$$

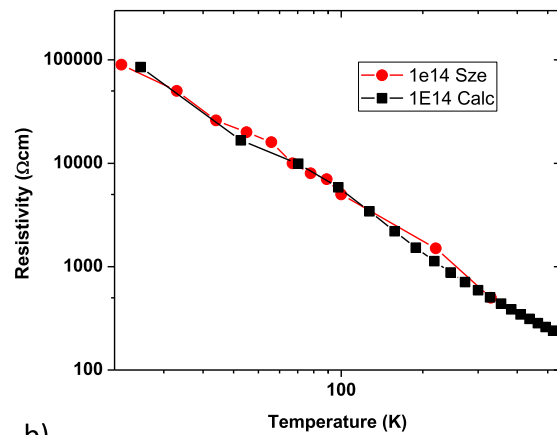
where $D(E)$ means the density of states for heavy holes (hh), light holes (lh), and split-off holes (so), respectively. Equation (16) can be solved iteratively, for instance, by the bisection method.

For further consideration of the Seebeck coefficient, we restrict the discussion of scattering effects to parabolic band structures and neglect the effect of mechanical stress.

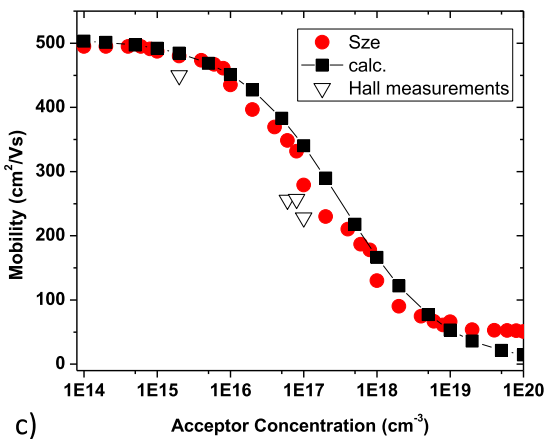
The prefactors $1/\tau_{ap0}$ [Eq. (7)], $1/\tau_{op0}$ [Eq. (9)], and $1/\tau_{ion0}$ [Eq. (12)] contain only physical constants found in different reference books. Therefore, they can be easily calculated. Some of the parameters applied for calculation differ, however, in different references. For instance, data for deformation potentials vary over a wide range. The acoustic deformation potential (D_{aph}) is specified as 2.2 eV,³⁸ 5.3 eV,³⁵ or 11 eV³⁹ resulting in values of $\tau_{ap0} = 7.4 \times 10^{-12}$, 2.5×10^{-13} , and 5.7×10^{-14} s, respectively. Furthermore,



a)



b)



c)

FIG. 1. Calculated data (black squares) for resistivity (a) and (b) and mobility (c) of p-type material (boron-doped) in dependence on the acceptor concentration and temperature. The data are compared to reference data given in the literature³⁷ (red full circles) and results of own Hall measurements of the mobility (open inverted triangles).

19 March 2024 07:16:39

data of the optical deformation potential (D_{oph}) vary between 5×10^8 eV/cm³⁸ and 6.6×10^8 eV/cm³⁴, yielding τ_{op0} between 1.5×10^{-13} and 8.5×10^{-14} s. Therefore, it is common to use $1/\tau_{ap0}$, $1/\tau_{op0}$, and $1/\tau_{ion0}$ as fit parameters for calculations of the conductivity according to Eq. (1).^{33,40} Variations provide indications on the effects of the individual parameters. It is shown that contributions by optical phonons and scattering on impurities are most important. The effect of impurity scattering is, however, less important even if incomplete ionization is assumed. For our calculations described below, we used $\tau_{ap0} \approx 4.3 \times 10^{-15}$ s, $\tau_{op0} = 1 \times 10^{-13}$ s, and $\tau_{in0} = 1 \times 10^{-8}$ s if the EPM method is applied to calculate the band structure. On the other hand, slightly different values of $\tau_{ap0} \approx 8 \times 10^{-15}$ s, $\tau_{op0} = 1 \times 10^{-13}$ s, and $\tau_{in0} = 1 \times 10^{-7}$ s were used by applying the $\mathbf{k} \cdot \mathbf{p}$ -method, which are close to data published by other authors.³³

Results of calculations of conductivity σ are represented in Figs. 1(a) and 1(b), where data of the resistivity (i.e., $1/\sigma$) are

plotted as a function of acceptor concentration and temperature. The resistivity is used instead of the conductivity for comparison with generally known reference data.³⁷ There is a good agreement with reference data over a whole range of impurity concentration and temperature, respectively. The same applies to mobility and their dependence on the acceptor concentration [Fig. 1(c)]. Furthermore, the Seebeck coefficient was calculated using Eq. (2) for a large range of impurity (acceptor) concentrations [Fig. 2(a)]. At a high acceptor level (10^{19} cm⁻³), S is about 0.5 mV/K at room temperature. The temperature dependence of the Seebeck coefficient is shown in Fig. 2(b) for different acceptor concentrations. The behavior of the calculated S on the impurity concentration and temperature agrees with experimental and theoretical data presented in the literature for bulk material and nanostructures.^{14,27,41-43} In addition, the power factor $S^2 \cdot \sigma$ as an important factor for the efficiency of a TEG is shown in Fig. 3.

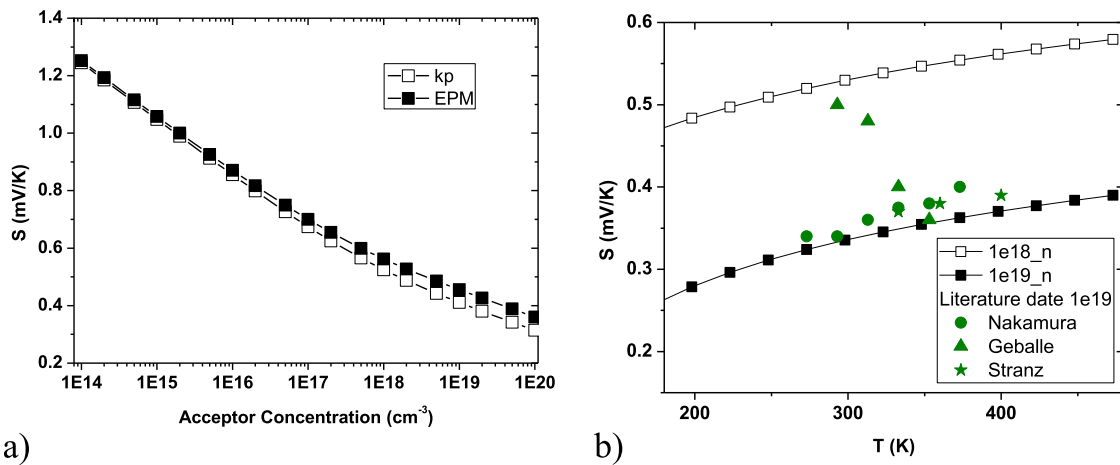


FIG. 2. (a) Calculated Seebeck coefficient in dependence on the acceptor concentration for room temperature. For band structure calculation, the EPM and $\mathbf{k} \cdot \mathbf{p}$ (6×6)-model were used. (b) Dependence of the calculated Seebeck coefficient on the temperature for acceptor concentrations of 1×10^{18} cm⁻³ (open squares) and 1×10^{19} cm⁻³ (full squares). Results are compared with literature data given by Nakamura²⁷ (full circles), Geballe and Hull (triangles, from Ref. 27), and Stranz *et al.*¹⁴ (stars).

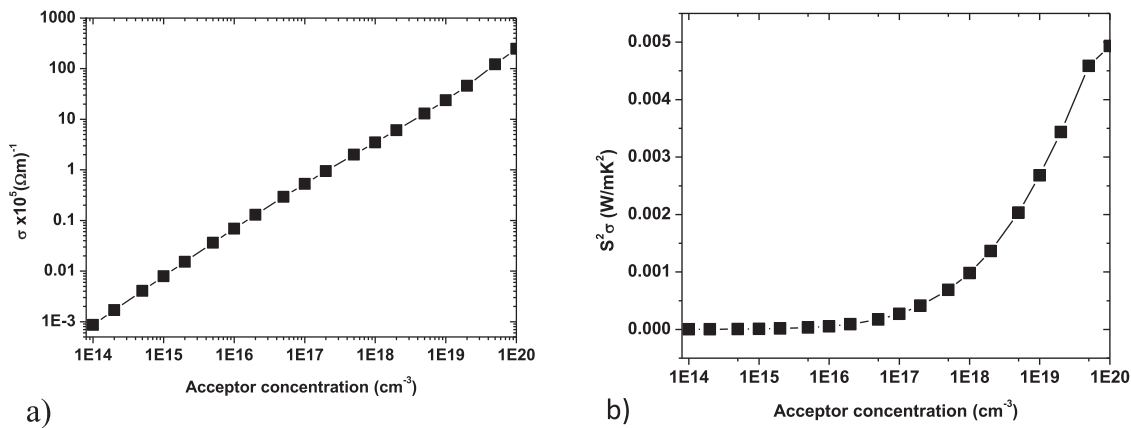


FIG. 3. Electrical conductivity (a) and power factor $S^2 \sigma$ as functions of acceptor concentration (b).

19 March 2024 07:16:39

III. DEVICE PREPARATION AND MEASUREMENT

Thermoelectric generators were realized by standard CMOS technology in a lateral geometry.^{5,44} All thermopiles are located on a thin membrane to reduce the heat flow. SOI wafers (device layers 25 μm thick (resistivity $\rho = 3\text{--}5 \Omega \text{ cm}$) and buried oxide thickness 200 nm, diameter 100 mm) were applied for experiments. In addition, bulk wafers with the same specification (resistivity, diameter) were used for comparison. To avoid short circuits in the case of n-type legs, p-type wells were prepared first by boron implantation (dose $3 \times 10^{13} \text{ cm}^{-2}$, energy 90 keV) followed by annealing at 1150 $^{\circ}\text{C}$ for 90 min. This results in p-wells of 3.5 μm depth having a boron concentration of about $1 \times 10^{18} \text{ cm}^{-3}$. Parallel n-type and p-type legs (width and distance 10 μm , respectively, lengths of 500, 1000, and 1500 μm) were fabricated within the p-type wells. For comparison, devices with both legs and only the n-type legs, respectively, were placed within the wells. Individual legs were realized by ion implantation of boron (90 keV) and phosphorous (140 keV) at different doses followed by annealing at 1000 $^{\circ}\text{C}$ for 30 min. This causes legs with depths of about 1.5 μm and boron and phosphorous concentrations, respectively, ranging from 7.5×10^{19} to $1.5 \times 10^{20} \text{ cm}^{-3}$. One end of individual pairs was connected to each other by a metal bridge (AlSi), while the other ends connect adjacent pairs. Finally, the handle wafer (SOI) or bulk material (bulk wafer) was removed from the backside by wet chemical etching resulting in devices with 30 or 46 pairs of thermopiles on thin membranes having thicknesses of 25 μm (SOI) or 30 μm (bulk wafer). The membrane sizes are $2.1 \times 0.75 \text{ mm}^2$. A plane view image of an individual device and details of a structure are shown in Fig. 4.

Both ends of the devices are mounted on Peltier elements to realize a hot side and a cold side. Temperatures on both sides were measured on-chip by calibrated diodes. A constant temperature difference of 20 or 30 K was adjusted.

The thermal stability of the devices was demonstrated by lock-in thermography. Figure 5 shows the amplitude image at a temperature difference of $\Delta T = 30 \text{ K}$ between the cold and hot sides. It is clearly shown that a stable temperature gradient exists over the thin membrane, where the red color characterizes the hot side. The reason is the reduced thermal conductivity by the reduction in the phonon contribution in consequence of a reduction in the mean free path. The reduction in the mean free path is obtained by increasing phonon scattering caused by decreasing dimensions of the material, either by thin films, nanowires,¹⁹ or in our case, by applying thin membranes. The effect of the thickness on the thermal conductivity across the membrane was studied by commercial Multiphysics simulation tools using standard material parameters (COMSOL⁴⁵). A model of the structure and corresponding temperature profiles across membranes with varying thickness are represented in Fig. 5 for $\Delta T = 30 \text{ K}$. Decreasing thickness from 200 μm down to 10 μm increases the temperature gradient at the membrane edges [Fig. 5(c)]. The temperature profiles for membrane thicknesses of 20 and 30 μm , however, are comparable with profiles calculated for 10 μm thick membranes.

Seebeck coefficients were measured for different devices using a previously described tool and procedure.⁴⁶ The thermovoltages by copper–constantan couples attached at both sides of the legs are measured. The results are corrected for the thermopower of

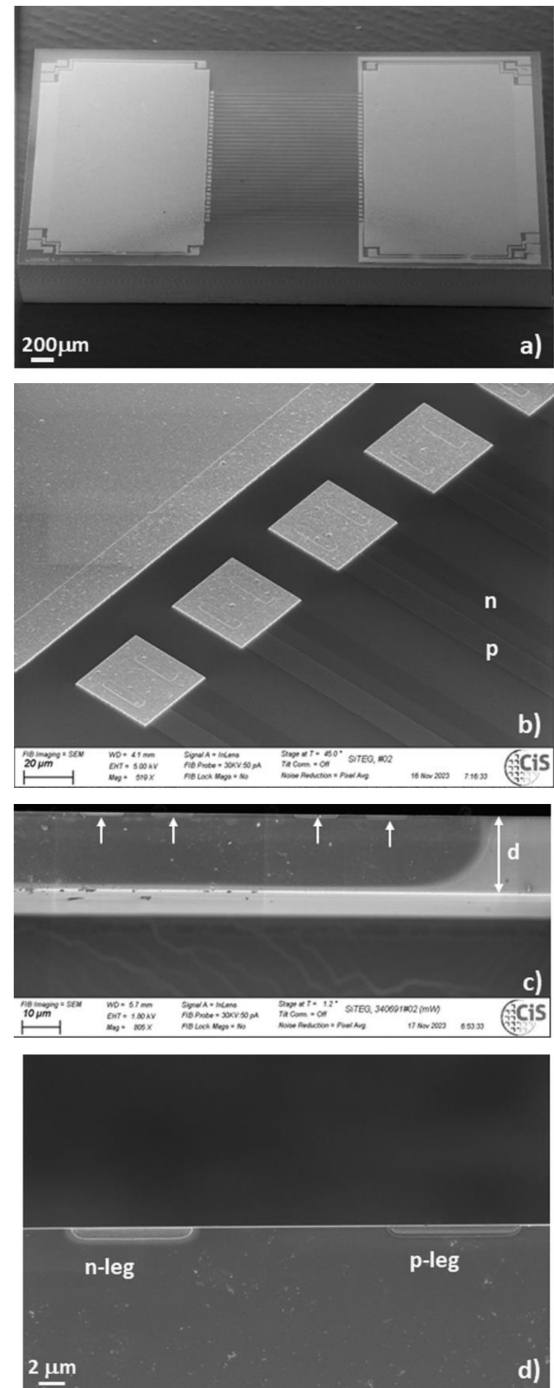


FIG. 4. Scanning electron microscope (SEM) plane view image of a device (a). The lengths of the legs are 500 μm . (b) An image at higher magnification shows individual n- and p-legs [indicated by n and p in (b)] and metal bridges (AlSi). SEM cross-section of a membrane (c). (d) The membrane thickness is 25 μm . The p-well is not visible under the applied image conditions. Arrows characterize the position of individual legs. Note that the image is slightly tilted resulting in the visibility of the backside of the membrane (visible as a bright strip in the image). (d) SEM cross-section at higher magnification shows a pair of n- and p-legs.

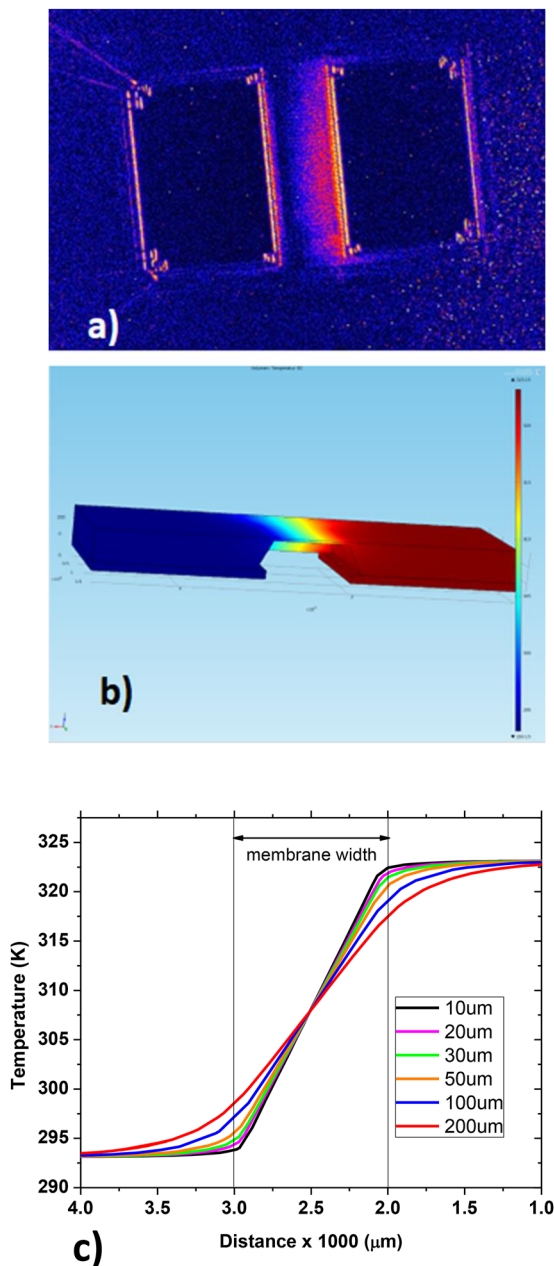


FIG. 5. Lock-in thermography (amplitude image) (a) of a device. The temperature gradient is 30 K. Red to yellow color indicates the high-temperature area. The blue color indicates the cold area. (b) The FEM model used for simulation of the temperature profile across the membrane. The different colors indicate the same temperature behavior. (c) Calculated temperature profiles are shown for different membrane thicknesses. The membrane width (1000 μm) is characterized by vertical lines.

the copper–constantan leads. A temperature difference of 5 K was adjusted. All measurements result in the Seebeck coefficient of individual legs (length 1000 μm , doping concentration $7.5 \times 10^{19} \text{ cm}^{-3}$) ranging from $S = 0.46 \text{ mV/K}$ to $S = 0.5 \text{ mV/K}$ at

room temperature. These data are in agreement with calculated ones (Fig. 2) and reference data given in the literature.^{14,27}

The open-circuit voltage (U_{OC}) reaches the highest values for devices with p- and n-legs within a p-well. Slightly reduced values of U_{OC} are obtained if only n-legs are in the p-well. For the first type (p- and n-legs in a p-well), an open-circuit voltage of 0.91 V is measured at a temperature difference of 20 K, while U_{OC} is only 0.88 V for the second type (only n-legs in a p-well). The doping level in both cases is the lowest one ($7.5 \times 10^{19} \text{ cm}^{-3}$) for p- and n-legs, respectively. The effect of different doping has been analyzed on devices prepared on bulk materials. The structures are also located on membranes (thickness 30 μm) and characterized by p- and n-legs within p-wells. Both legs have lengths of 1500 μm , and 46 thermopile pairs exist. Measurements proved a strong dependence of U_{OC} on the doping level of both types of legs. Increasing the doping level of p- and n-type legs decreases the open-circuit voltage. The highest values of U_{OC} are obtained for the lowest concentrations for p- and n-type legs ($7.5 \times 10^{19} \text{ cm}^{-3}$). Furthermore, U_{OC} depends also on the lengths of the legs. Devices having lengths of the legs of 1000 μm result in the highest open-circuit voltages, while smaller 500 μm or larger (1500 μm) are characterized by lower values of U_{OC} .

Based on measurements of open-circuit voltage and short-circuit current, a resistivity of about $2.98 \times 10^{-3} \Omega \text{ cm}$ follows for an individual thermopile pair corresponding to a conductivity ($\sigma = 1/R$) of $0.345 \times 10^5 \text{ A/V m}$. Furthermore, using the experimentally determined Seebeck coefficient $S = 0.46 \text{ mV/K}$, the power factor is $S^2 \cdot \sigma = 0.0073 \text{ W/mK}^2$, which is in good agreement with the computed value [cf. Fig. 3(b)].

For practical applications, a thermoelectric generator is intended to operate between hot and cold thermal reservoirs, both with a constant temperature. The heat flow through the TEG is small enough to have a negligible effect on the temperature of the two reservoirs. In such a case, the efficiency of the thermoelectric generator is much less important than how much electrical power per unit cross-section area for heat flow a TEG can produce from the temperature difference $\Delta T = T_H - T_C$ between the hot (T_H) and cold reservoir (T_C). The maximum power

$$P_{\max} = \frac{1}{4} (U_{OC} I_{sc}) \quad (17)$$

a TEG produces is proportional to $(\Delta T)^2$ and to the cross-sectional area A . Thus, the specific power generation capacity,⁹ or the efficiency factor,⁴⁷

$$\Gamma_P = \frac{P_{\max}}{A \cdot (\Delta T)^2}, \quad (18)$$

is more important than the efficiency. Γ_P is a circuit characteristic parameter and can be increased, for instance, by using a large number of thermopile pairs per unit area. P_{\max} was measured at $\Delta T = 10 \text{ K}$ to be 0.012–0.138 μW for devices with leg lengths of 500 μm . This corresponds to previously reported data measured on silicon thermoelectric generators.⁹

Normalizing to the cross-sectional area A , then according to Eq. (18), a specific power generation capacity Γ_P between 6.67 and 2.26 $\mu\text{W cm}^{-2} \text{ K}^{-2}$ results for the different TEG variants at $\Delta T = 10 \text{ K}$. This is equivalent to nanostructured silicon thermopiles and competitive with typical $(\text{Bi,Sb})_2(\text{Se,Te})_3$ -based TEGs.¹³

Because Γ_P is indirectly proportional to the cross-sectional area and temperature difference, increasing A or ΔT results in a reduction of the power generation capacity and should be as small as possible.

Furthermore, an indicator of the performance of micro thermoelectric generators is the relation between the specific power generation capacity and the design parameter A_V , which is the ratio of cross-sectional areas of insulation (or chip, A_I) to active material (A_0) in the plane perpendicular to the heat flow. A linear dependence is obtained between Γ_P and A_V in a double logarithmic reference frame for different materials.⁴⁷ In our case, $A_I = 0.025 \text{ cm}^2$ and $A_0 = 3.6 \times 10^{-4} \text{ cm}^2$, resulting in

$$A_V = \frac{A_I}{A_0} = 69.4. \quad (19)$$

The linear dependence according to Ref. 47 refers to $\Gamma_P \approx 0.3 \mu\text{W cm}^{-2} \text{ K}^{-2}$ for $A_V = 69.4$ and is about a factor of ten below the measured value. The difference may be caused by differences between the test and harvest mode.¹³

IV. CONCLUSIONS

A theoretical model describing electric and thermoelectric properties especially of highly doped p-type silicon is presented. The model is based on the Kubo–Greenwood formalism. The model includes band structure calculations using the empiric pseudopotential method (EPM) or by a $\mathbf{k} \cdot \mathbf{p}$ (6×6)-method. Contrary to previous papers,³³ we consider parts for scattering of acoustic phonons, nonpolar optical phonons, and scattering on ionized impurities individually for each valence band. The validity of the model was proved by calculations of the resistivity and carrier mobility in dependence on the acceptor concentration and temperature.

The model was used to calculate the Seebeck coefficient S , the electrical conductivity σ , and the power factor $S^2\sigma$ in dependence on the acceptor concentration. The temperature dependence of the calculated Seebeck coefficient agrees with previously published experimental and computed data given in the literature.^{14,27}

Test devices of micro thermoelectric generators are prepared using the standard CMOS technology in a lateral-type design.⁴⁷ All thermopiles are located on a thin membrane (thickness of 25 or 30 μm) to reduce the heat flow. Thermography measurements and calculations of the thermal conductivity proved stable temperature gradients across the thin membranes. A Seebeck coefficient of $S = 0.46 \text{ mV/K}$ to $S = 0.5 \text{ mV/K}$ was measured on devices and is in good agreement with the computed one for an acceptor concentration of $7.5 \times 10^{19} \text{ cm}^{-3}$. The same holds for the power factor $S^2\sigma$. The determined specific power generation capacity, or efficiency factor, Γ_P is between 6.68 and $2.26 \mu\text{W cm}^{-2} \text{ K}^{-2}$ for TEGs considered. The values are comparable to those measured on nanostructured Si TEGs and thermoelectric generators realized on materials having the best data for the figure-of-merit (ZT).^{9,13}

ACKNOWLEDGMENTS

This work was financially supported by the German Federal Ministry for Economic Affairs and Climate Action (Grant Nos. 49VF180038 and VF120014). We thank N. Buczek (T. H. Lübeck) for supporting the Seebeck measurements.

AUTHOR DECLARATIONS

Conflict of Interest

The authors have no conflicts to disclose.

Author Contributions

Hartmut Uebensee: Software (lead); Writing – review & editing (equal). **Manfred Reiche:** Data curation (equal); Investigation (equal); Writing – original draft (lead). **Hans Kosina:** Methodology (equal); Software (equal); Writing – review & editing (equal). **Xue-mei Xu:** Data curation (lead); Validation (equal); Writing – review & editing (equal). **Hartmut S. Leipner:** Conceptualization (equal); Investigation (equal); Validation (equal); Writing – review & editing (equal). **Geert Brokmann:** Conceptualization (equal); Formal analysis (equal); Project administration (equal); Validation (equal). **Bernhard Schwartz:** Formal analysis (equal); Software (equal); Validation (equal); Writing – review & editing (equal). **Anna Reinhardt:** Data curation (equal); Investigation (equal); Resources (equal); Visualization (equal); Writing – review & editing (equal). **Thomas Ortlepp:** Conceptualization (equal); Funding acquisition (equal); Project administration (lead); Supervision (equal); Writing – original draft (equal).

DATA AVAILABILITY

The data that support the findings of this study are available on request from the corresponding author.

REFERENCES

- D. M. Rowe, *Thermoelectric Handbook* (CRC Press, Boca Raton, 2006).
- H. J. Goldsmid, *Introduction to Thermoelectricity*, 2nd ed. (Springer, Berlin, 2016).
- G. J. Snyder and E. S. Toberer, *Nat. Mater.* **7**, 105 (2008).
- A. Shakouri, *Annu. Rev. Mater. Res.* **41**, 399 (2011).
- J. Yan, X. Liao *et al.*, *J. Microelectromech. Syst.* **27**, 1 (2018).
- J. H. Oh, M. Shin, and M.-G. Jang, *J. Appl. Phys.* **111**, 044304 (2012).
- A. I. Hochbaum, R. Chen, R. D. Delgado, W. Liang, E. C. Garnett, M. Najarian, A. Majumdar, and P. Yang, *Nature* **451**, 163 (2008).
- A. I. Boukai, Y. Bunimovich, J. Tahir-Kheli, J.-K. Yu, W. A. Goddard III, and J. R. Heath, *Nature* **451**, 168 (2008).
- M. Lee, *J. Supercond. Novel Magn.* **33**, 253 (2020).
- N. Neophytou, V. Vargiamidis, S. Foster, P. Graziosi, L. de Sousa Oliveira, D. Chakraborty, Z. Li, M. Thesberg, H. Kosina, N. Bennett, G. Pennelli, and D. Narducci, *Eur. Phys. J. B* **93**, 213 (2020).
- N. Neophytou, *Eur. Phys. J. B* **88**, 86 (2015).
- V. Vargiamidis and N. Neophytou, *Phys. Rev. B* **99**, 045405 (2019).
- G. Hu, H. Edwards, and M. Lee, *Nat. Electron.* **2**, 300 (2019).
- A. Stranz, J. Kähler, A. Waag, and E. Peiner, *J. Electron. Mater.* **42**, 2381 (2013).
- N. Neophytou, X. Zianni, H. Kosina, S. Frabboni, B. Lorenzi, and D. Narducci, *Nanotechnology* **24**, 205402 (2013).
- Y. Ohishi, J. Xie, Y. Miyazaki, Y. Aikebaier, H. Muta, K. Kurosaki, S. Yamanaka, N. Uchida, and T. Tada, *Jpn. J. Appl. Phys.* **54**, 071301 (2015).
- D. Narducci and F. Giulio, *Materials* **15**, 1214 (2022).
- T.-M. Bah, S. Didenko, S. Monfray, T. Skotnicki, E. Dubois, and J.-F. Robillard, paper presented at the Proceedings of the 48th European Solid-State Device Research Conference (ESSDERC), Dresden, 2018.
- M. Haras, V. Lacatena, F. Norini, J.-F. Robillard, S. Monfray, T. Skotnicki, and E. Dubois, *IEDM Tech. Digest* **2014**, 8.5.1 (2014).

- ²⁰Q. Hao, G. Zhu, G. Joshi, X. Wang, A. Minnich, Z. Ren, and G. Chen, *Appl. Phys. Lett.* **97**, 063109 (2010).
- ²¹H. Li, Y. Yu, and G. Li, *J. Appl. Phys.* **115**, 124316 (2014).
- ²²A. J. Minnich, M. S. Dresselhaus, Z. Ren, and G. Chen, *Energy Environ. Sci.* **2**, 466 (2009).
- ²³L. D. Hicks and M. S. Dresselhaus, *Phys. Rev. B* **47**, 12727 (1993).
- ²⁴N. Neophytou and H. Kosina, *J. Electron. Mater.* **41**, 1305 (2012).
- ²⁵V. di Stefano and O. Muscato, *Acta Appl. Math.* **122**, 225 (2012).
- ²⁶Z. Wang, S. Wang, S. Obukhov, N. Vast, J. Sjakste, V. Tyuterev, and N. Mingo, *Phys. Rev. B* **83**, 205208 (2011).
- ²⁷K. Nakamura, *Jpn. J. Appl. Phys.* **55**, 06GJ07 (2016).
- ²⁸R. Kubo, *Can. J. Phys.* **34**, 1274 (1956).
- ²⁹D. A. Greenwood, *Proc. Phys. Soc.* **71**, 585 (1958).
- ³⁰E. Ungersboeck, PhD thesis, Technische Universität Wien, Vienna, 2007.
- ³¹F. Ungersboeck, V. Sverdlov, H. Kosina, and S. Selberherr, in *ECS Trans.* (The Electrochem. Society, Pennington, 2006), Vol. 4.
- ³²Z. Chao, X. Da-Qing, L. Shu-Lin, and L. Ning-Zhuang, *Adv. Condens. Matter Phys.* **2014**, 686303 (2014).
- ³³J. Richter, J. Pedersen, M. Brandbyge, E. V. Thomsen, and O. Hansen, *J. Appl. Phys.* **104**, 023715 (2008).
- ³⁴M. Hackel, Ph.D. thesis, Techn. University, Viena, 1995.
- ³⁵B. K. Ridley, *Quantum Processes in Semiconductors*, 4th ed (Clarendon Press, Oxford, 1999).
- ³⁶M. Reiche and H. Uebensee, *Quantum effects in MEMS sensors*, 49VF180038, CIS Erfurt, 2021.
- ³⁷S. M. Sze and K. K. Ng, *Physics of Semiconductor Devices*, 3rd ed. (Wiley, Hoboken, 2007).
- ³⁸C. Jacoboni, C. Canali, G. Ottaviani, and A. Alberigi Quaranta, *Solid-State Electron.* **20**, 77 (1977).
- ³⁹R. Paul, *Halbleiterphysik*, 1st ed. (Verlag Technik, Berlin, 1974).
- ⁴⁰F. Szmulowicz, *Appl. Phys. Lett.* **43**, 485 (1983).
- ⁴¹W. Fulkerson, J. P. Moore, R. K. Williams, R. S. Graves, and D. McElroy, *Phys. Rev.* **167**, 765 (1968).
- ⁴²N. Neophytou and H. Kosina, *J. Appl. Phys.* **112**, 024305 (2012).
- ⁴³F. Salleh, K. Asai, A. Ishida, and H. Ikeda, *Appl. Phys. Express* **2**, 071203 (2009).
- ⁴⁴H. Übensee, M. Reiche, and E. Hiller, paper presented at the 7. GMM-Workshop, Magdeburg, 2014.
- ⁴⁵Comsol, Comsol Multiphysics, <https://www.comsol.de>.
- ⁴⁶K. Bertram, M. Stordeur, F. Heyroth, and H. S. Leipner, *J. Appl. Phys.* **106**, 063711 (2009).
- ⁴⁷W. Glatz, E. Schwyter, L. Durrer, and C. Hierold, *J. Microelectromech. Syst.* **18**, 763 (2009).